Size-Dependent Nanoscale Kirkendall Effect During the Oxidation of Nickel Nanoparticles

Justin G. Railsback, Aaron C. Johnston-Peck, Junwei Wang, and Joseph B. Tracy*

Department of Materials Science and Engineering, North Carolina State University, Raleigh, North Carolina 27695

ARTICLE

ABSTRACT The transformation of Ni nanoparticles (NPs) of different sizes (average diameters of 9, 26, and 96 nm) during oxidation to hollow (single void) or porous (multiple voids) NiO through the nanoscale Kirkendall effect was observed by transmission electron microscopy. Samples treated for 1—4 h at 200—500 °C show that the structures of the completely oxidized NPs do not depend on the temperature, but oxidation proceeds more quickly at elevated temperatures. For the Ni/NiO system, after formation of an initial NiO shell (of thickness ~3 nm), single or multiple voids nucleate on the inner surface of the NiO shell, and the voids grow until conversion to NiO is complete. Differences in the void formation and growth processes cause size-dependent nanostructural evolution: For 9 and 26 nm NPs, a single void forms beneath the NiO shell, and the void grows by moving across the NP while conversion to NiO occurs opposite the site where the void initially formed. Because of the differences in the Ni/NiO volume ratios for the 9 and 26 nm NPs when the void first forms, they have distinct nanostructures: The 9 nm NPs form NiO shells that are nearly radially symmetric, while there is a pronounced asymmetry in the NiO shells for 26 nm NPs. By choosing an intermediate oxidation temperature and varying the reaction time, partially oxidized Ni(core)/NiO(shell) NPs can be synthesized with good control. For 96 nm NPs, multiple voids form and grow, which results in porous NiO NPs.

KEYWORDS: Kirkendall effect · nanoparticle · nickel · nickel oxide · hollow nanoparticles · diffusion

The Kirkendall effect, a vacancy flux and subsequent void formation resulting from diffusivity differences at inorganic interfaces, was first reported for nanoparticles (NPs) in 2004,[1] when solid metal NPs were converted to hollow metal oxide, sulfide, and selenide NPs. Such conversions through the Kirkendall effect are known as the nanoscale Kirkendall effect (NKE), in which the reduced dimension of the material imposes boundary conditions on the conversion process. Some examples of hollow nanostructures formed through the NKE include CoS,[1,2] CoO,[1,3−5] CoSe,[1,6] Fe_xO_y,[7−9] Al_2O_3,[10,11] Cu_2O,[9,10,12] ZnO,[11,13] Ni_2P,[14−17] Co_2P,[18] CoP,[14−16] CdS,[19,20] and NiO.[9,21] Typically, a unary metal NP is exposed to oxygen, phosphorus, sulfur, or selenium precursors under elevated temperatures resulting in a diffusion couple. When outward diffusion of the metal cations is much faster than the inward diffusion of the anions, an inward flux of vacancies accompanies the outward metal cation flux to balance the diffusivity difference. When the vacancies supersaturate, they coalesce into a void (or in some cases, several small voids that usually merge into a larger void);[1,2,9,21,22] the reaction products are hollow NPs with binary compositions. Strain at the interface may also aid void formation.[23] Hollow metal-oxide NPs have frequently been synthesized by reactions in solution or oxidation in air at elevated temperatures.[1−6,8,10−16,18,21] These hollow NPs are attractive for their potential use in catalysis,[24,25] energy storage,[5,26,27] and biomedical applications[28,29] owing to their high surface area to volume ratio and internal void morphology. Partially oxidized magnetic NPs are also of interest due to magnetic exchange coupling between the core and shell, which provides opportunities to control the magnetic properties of heterostructured NPs.[3,30−37]

In the NKE, voids usually form at the inside of the core/shell interface and then grow until conversion is complete.[22] The number of voids and the mechanism of void growth depend on the relative rates of self-diffusion in the core material versus cation diffusion through the shell:[21] if self-diffusion is fast, then a single void may form and grow until conversion is complete (*e.g.*, NiO).[21] Alternatively, if self-diffusion is significantly slower than cation diffusion through the shell, then several voids remain, and multiple bridges form that connect the shrinking core to the shell as the voids grow and finally combine into a symmetrical void[2,22] (*e.g.*, CoO,[1,5] Co_xS_y,[1,2] and Fe_xO_y).[8]

*Address correspondence to jbtracy@ncsu.edu.

Received for review November 30, 2009 and accepted March 17, 2010.

Published online April 2, 2010.
10.1021/nn901736y

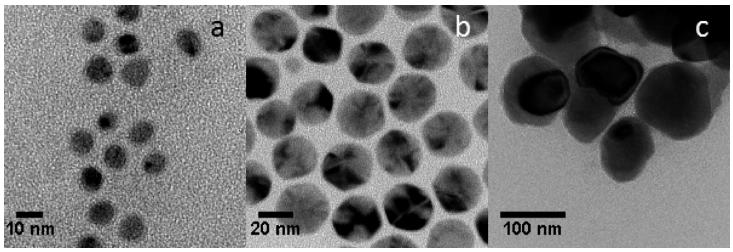

Figure 1. Ni nanoparticles after exposure to air at room temperature and ligand removal. The average dimensions for each nanoparticle are (a) 5.8 nm core, 1.6 nm shell; (b) 23.4 nm core, 1.3 nm shell; (c) 88.2 nm core, 3.9 nm shell.

Here, we report and discuss the mechanism of the *size-dependent* NKE during the oxidation of Ni NPs in air to form hollow (single void) or porous (multiple voids) partially or completely oxidized Ni/NiO NPs at different temperatures and times. There are marked differences in the symmetric, asymmetric, and porous nanostructures that are obtained from different sizes of Ni NPs.

RESULTS AND DISCUSSION

Ligand-stabilized Ni NPs with average diameters of 9, 26, and 96 nm were synthesized and drop cast onto SiO support films on Cu grids for transmission electron microscopy (TEM), for which images are shown in Figure 1. SiO supports were chosen rather than amorphous carbon, because SiO is more durable and deforms less during the heat treatments than carbon. The 96 nm NPs were prone to agglomeration due to their limited solubility and potentially attractive interparticle magnetic interactions. The ligands were removed by cleaning with ultraviolet light and ozone (UVO)[38−40] as a precaution to separate any possible effects of thermal ligand desorption from the oxidation process. Minimal oxidation occurs in air at room temperature,[41] and the NiO shell thicknesses were measured by TEM. Results for the oxidation of the Ni NPs at 200−500 °C for 1−4 h are presented in Figures 2−4. (For each sample, corresponding electron diffraction is provided in the Supporting Information, Figures S-1−4.) The increased temperatures induce mobility of the NPs on the substrate, which can lead to agglomeration. For most samples, agglomeration during oxidation was not severe, and many isolated NPs were still observed.

Role of Temperature. In our previous study,[41] amorphous NiO shells were observed at 200 °C, which is consistent with the smooth, thin NiO shells observed here before void formation. At higher temperatures after complete oxidation, the appearance of the shells is lumpy rather than smooth (Figures 2i, 3f, and 4f), and the corresponding SAED (Supporting Information, Figures S-2i, S-3f, and S-4f) shows that the shells crystallize as NiO with the rocksalt structure. The NiO shells have significantly crystallized for some samples already at 300 °C (Figure 2f) and for all samples when heated at 400 °C for longer than an hour. Outward diffusion of Ni through NiO grains and grain boundaries could provide additional driving force for crystallization, but it is also plausible that crystallization of the NiO shells could have a role in causing void formation.

In principle, different intermediate and final structures might be accessible at different temperatures, because the NKE is controlled by diffusion.[2] The relative rates of self-diffusion of the core material compared to its diffusion through the shell could strongly depend on temperature. For each size, the oxidized structures for all temperatures are quite similar, however, which implies that the conversion mechanism does not significantly depend on

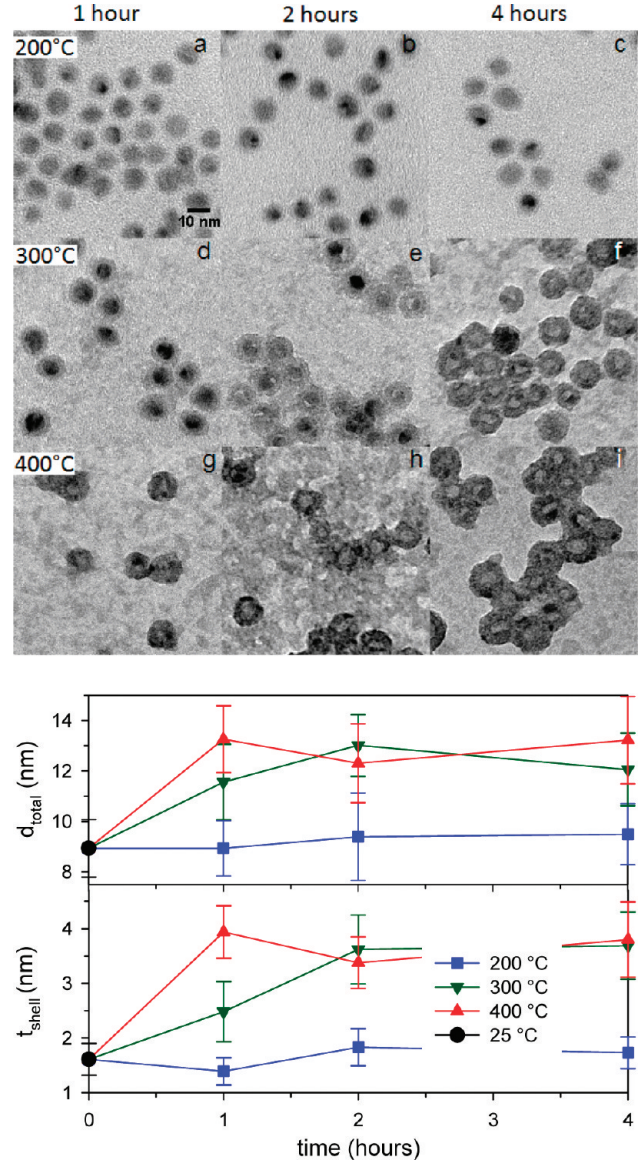

Figure 2. Top panel: TEM images of 9 nm oxidized Ni nanoparticles. Columns from left to right: 1, 2, and 4 h; rows from top to bottom: 200, 300, and 400 °C. Bottom panel: plots of the average outer diameters (d_{total}) and shell thicknesses (t_{shell}) for different temperatures and times.

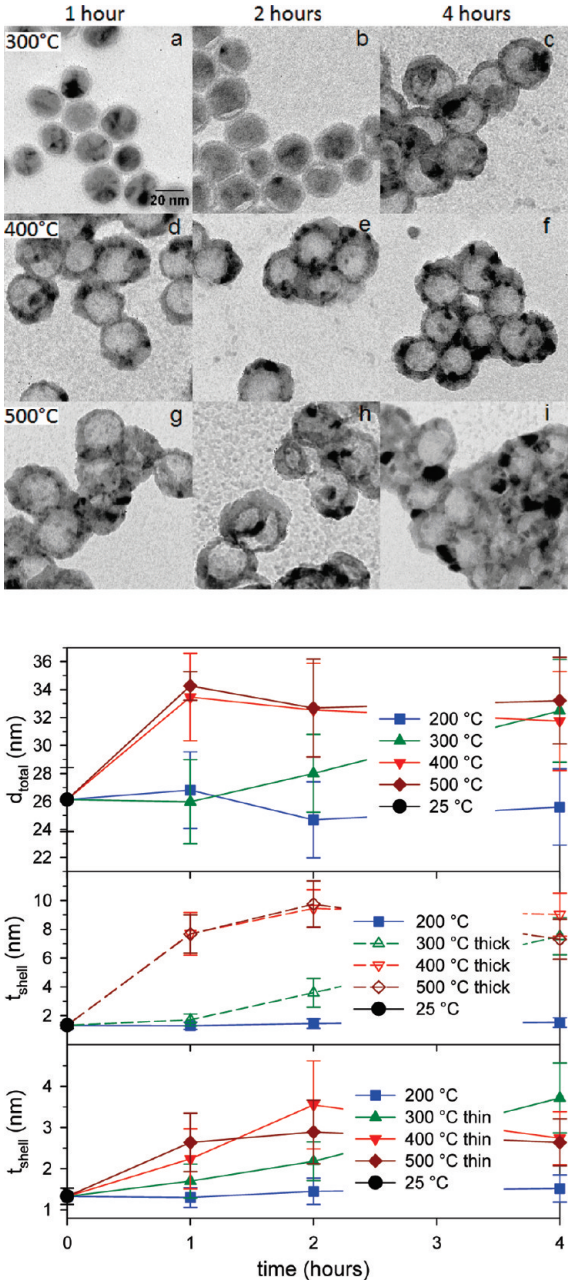

Figure 3. Top panel: TEM images of 26 nm oxidized Ni nanoparticles. Columns from left to right: 1, 2, and 4 h; rows from top to bottom: 300, 400, and 500 °C. Bottom panel: plots of the average outer diameters (d_{total}) and average shell thicknesses (t_{shell}) for different temperatures and times. Void formation for temperatures greater than 200 °C introduced significant asymmetry into the shell, and measurements of t_{shell} at its thickest and thinnest points are plotted separately. (TEM images for samples treated at 200 °C are provided in the Supporting Information, Figure S-5.)

temperature, even though the conversion rate strongly depends on temperature. For this reason, whether the ligands are removed prior to heat treatment or are left intact is expected to have minimal effect on the products. Ligand desorption or pyrolysis would occur below 500 °C,[42−44] higher oxidation temperatures (but not above 500 °C) might be required if the ligands were left intact, but the final structures would be the same as reported here.

Nanoparticle Morphology. For the 9 and 26 nm Ni NPs, a single large void usually forms at the core/shell interface (Figures 2e,f, and 3b,c) and grows until the particles are completely converted to NiO. The 9 nm NPs remain approximately symmetrical, while the 26 nm NPs exhibit off-center spherical voids, nonuniform shell thicknesses, and asymmetrical NP shapes. Results for the process of void growth at 300 °C and graphical depictions of the origins of asymmetry are presented in Figure 5. (Corresponding electron diffraction and an additional TEM image of partially oxidized NPs are provided in the Supporting Information, Figures S-7−8 and S-9, respectively.) Analysis of HRTEM images (Figure 6 and Supporting Information, Figure S-10) confirms that lattice spacings for Ni correspond to the core, while lattice spacings for NiO are observed for the shells. (We note that in TEM images, the shell can overlap with the core, because TEM shows a two-dimensional projection of a three-dimensional object.) As described in the Introduction, single voids are expected for the Ni/NiO system because the rates of Ni self-diffusion and diffusion in NiO are similar, which provides ample mobility for vacancies to coalesce into a larger void before Ni transport through the NiO layer is complete.[21,45,46]

As the conversion of 9 and 26 nm NPs proceeds, the NiO shell adjacent to the void (opposite to the Ni core) grows only negligibly, which implies minimal lateral diffusion of Ni within the NiO layer. Some images (Figures 2e,f and 3c−f) show that the Ni core assumes an approximately spherical shape toward the end of the oxidation process. For the 26 nm NPs, the Ni core initially diffuses quickly into the NiO shell where the Ni core already has an interface with the NiO shell, which leaves a ball of material that slowly diffuses through the small remaining Ni/NiO interface. If the Ni/NiO interface would fracture, a small solid Ni NP would remain inside of the hollow NiO NP, and outward Ni diffusion would become less effective, due to the loss of the fixed Ni/NiO interface. Such a phenomenon may occur for Ni_2P NPs, in which a loose solid or hollow spherical NP is contained inside a hollow Ni_2P NP.[15]

As the Ni core converts to NiO, the NiO is deposited opposite the void. After complete oxidation, the NiO shell is thinnest adjacent to the point where the void nucleated and remains the same thickness as when the void was first formed. The NiO shell is thickest opposite to the void, because the core Ni diffuses away from the void as it is oxidized. Therefore, the asymmetry in the shell is controlled by the ratio $R = V_{Ni}/(V_{Ni} + V_{NiO})$, where V is the volume of each phase *when the void first forms*, which is the time at which the NP first becomes asymmetrical. Larger values of R correspond to greater relative proportions of reduced Ni and give greater asymmetry. This ratio is much greater for the 26 nm NPs than for the 9 nm NPs, as calculated from TEM measurements of the core diameters, where both the cores and NPs are treated as spheres, and then calculating the core and to-

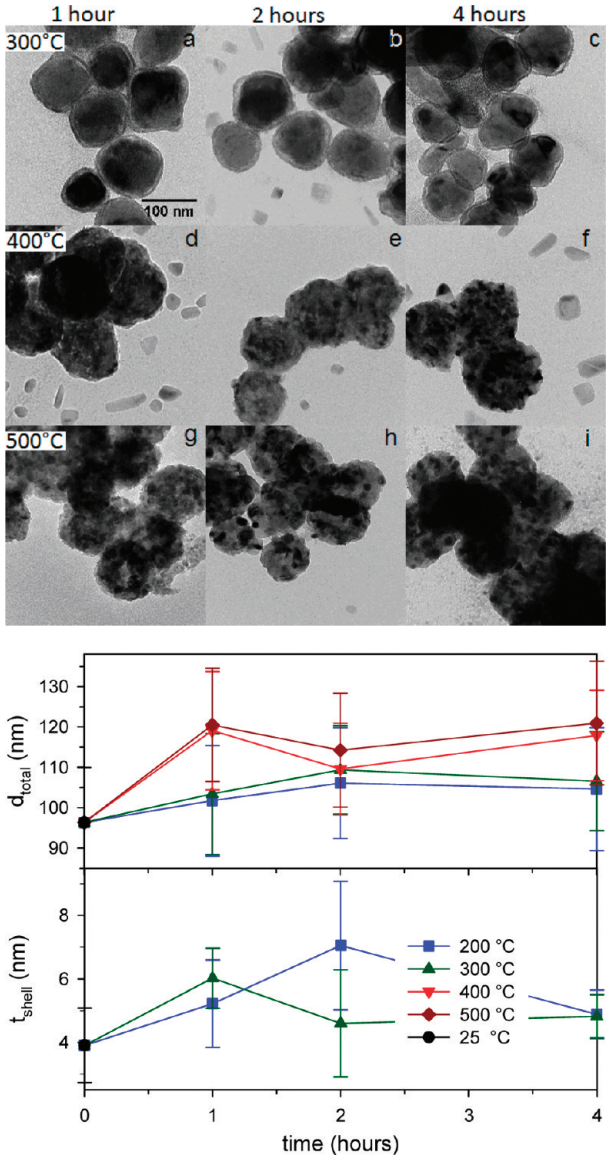

Figure 4. Top panel: TEM images of 96 nm oxidized Ni nanoparticles. Columns from left to right: 1, 2, and 4 h; rows from top to bottom: 300, 400, and 500 °C. Bottom panel: plots of the average outer diameters (d_{total}) and shell thicknesses (t_{shell}) for different temperatures and times. The shell thicknesses could be measured only at 200 and 300 °C. (TEM images for samples treated at 200 °C are provided in the Supporting Information, Figure S-6.)

tal volumes, $V = (4\pi/3)(d/2)^3$. For example, at 300 °C and 1 h, the average core/total diameters of the 9 nm NPs are 6.6 nm/11.6 nm and are 22.6 nm/26.0 nm for the 26 nm NPs, which gives $R_{9\ nm} = 0.19$, and $R_{26\ nm} = 0.66$. After complete oxidation, the void has a striking resemblance to the Ni core after initial NiO shell growth but before void formation, which is consistent with minimal inward diffusion of oxygen and growth exclusively by core Ni atoms diffusing through the existing Ni/NiO interface.

The structural changes when converting 96 nm Ni NPs to NiO are substantially different, because Ni self-diffusion over the larger NP size does not prevent formation of multiple voids at the Ni/NiO interface (Figure 4a−c). Self-diffusion of Ni is not fast enough to condense all the vacancies into a single void. At the early stages of oxidizing 96 nm NPs, the voids are shallow and cover a large portion of the Ni/NiO interface (Figure 4b,c). The simultaneous growth of multiple voids results in a porous structure rather than a large, single void. Crystallization of NiO grains for the 96 nm NPs is particularly distinct. When the treatment temperature and time are increased to 400 °C for 4 h or 500 °C for 2 h, the average NiO grain size in the final oxidized structure increases to ~20 nm.

There have been reports of nanostructural transformations driven by the electron beam during TEM measurements, which have included NP sintering[47,48] and void formation.[49,50] In our experiments, TEM imaging was performed using standard bright-field techniques, and there was no evidence for electron beam-induced effects. Rather, the oxidation temperature and time determined the extent of conversion and the nanostructure.

Critical Shell Thickness for Void Formation. Before performing oxidation reactions but after UVO treatment, the native NiO shell thickness (t_{native}) for the 96 nm sample is substantially greater than for the 9 and 26 nm samples (Table 1). The origin of this difference is unclear, because differences in the synthetic procedures (specifically, the use of trioctylphosphine for the 9 and 26 nm sizes but not for the 96 nm size) could cause differences in the ligand stabilization that would influence the formation of the native oxide prior to ligand removal. Our prior results indicate that the native oxide forms while the ligands are present,[41] and we have not observed further oxidation caused by UVO treatment at room temperature.

During heating in air, the NiO shell first grows thicker, until the critical shell thickness for void formation ($t_{critical}$) is reached (Table 1). Measurements of $t_{critical}$ do not depend on the oxidation temperature (variations for different temperatures are contained within the error of the measurement of $t_{critical}$), which is consistent with our observation that the oxidation temperature affects only the reaction rate and not the reaction mechanism. There is a clear trend that $\Delta t = t_{critical} - t_{native}$ decreases as the NP size increases. This trend is supported by two geometry effects, if growth of the native oxide is through inward diffusion of oxygen (with minimal outward diffusion of Ni) at room temperature, which is a reasonable assumption: (1) As the size increases, the surface area of the core/shell interface per NP increases, and a greater number of vacancies are generated for a given increase in the shell thickness. Vacancies throughout the whole NP (or from regions of the NP for the 96 nm NPs) coalesce into the void. If the number of vacancies required to form the void is not strongly size dependent, then a larger NP favors void formation for smaller Δt. (2) As the NP size decreases, the core/shell interface is no longer approximated by a

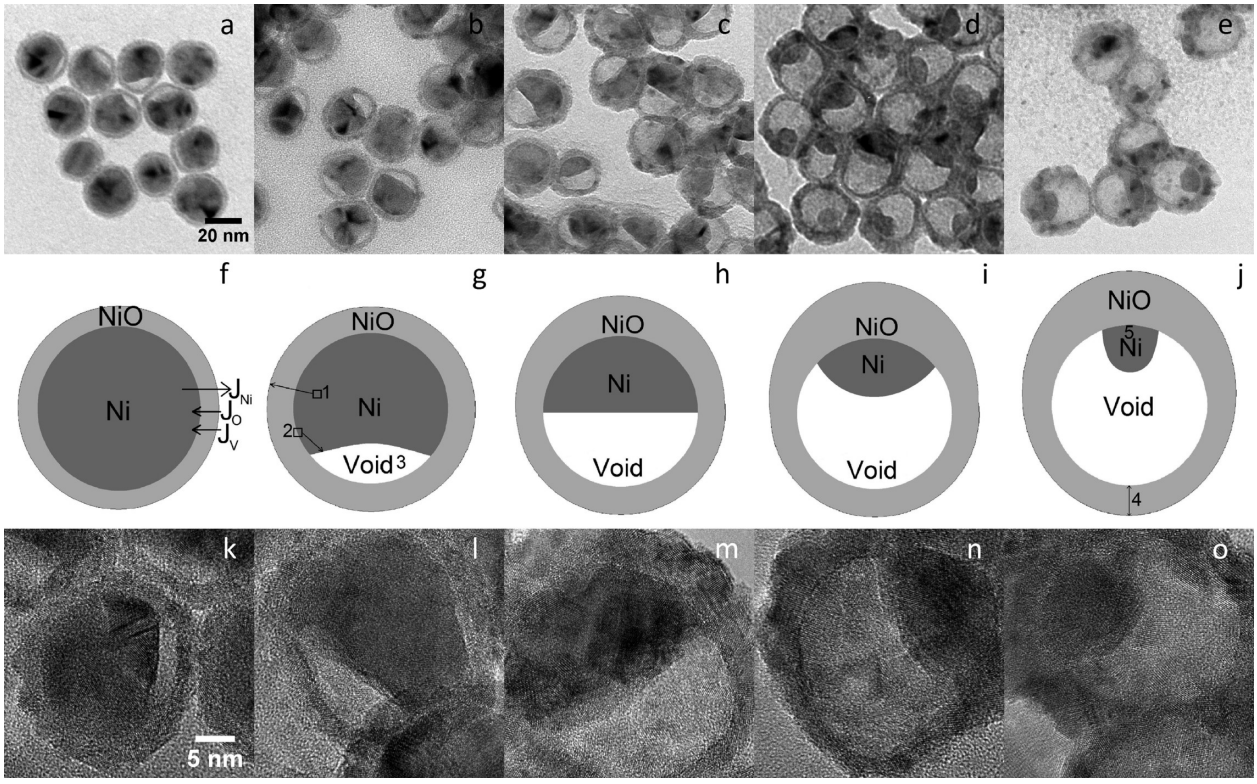

Figure 5. TEM images of 26 nm nanoparticles after oxidation in air at 300 °C for (a) 90, (b) 120, (c) 150, (d) 180, and (e) 210 min. Corresponding oxidation schemes and high-resolution TEM images are shown below (a−e). (g−j) (1) Nickel diffuses across the Ni/NiO interface only and (2) vacancies are injected at the interface and diffuse to the void. (3) The void nucleates when vacancies supersaturate. (4) The shell remains the same thickness where the void nucleated, because little lateral Ni diffusion occurs along the void/shell interface or in the NiO shell. (5) Toward the end of oxidation, the core becomes a small ball whose oxidation might be slowed by the reduced Ni/NiO interfacial area and the thick NiO layer through which Ni cations must diffuse.

planar interface, and the Ni must diffuse radially in all outward directions, while oxygen diffuses inward from all directions. Therefore, the smaller radius of curvature for smaller NPs favors inward diffusion of oxygen and inhibits outward diffusion of Ni, and a larger Δt is expected for smaller sizes, because a thicker NiO shell must be grown before enough vacancies are available to form a void. Formation of multiple voids for 96 nm NPs does not violate this trend.

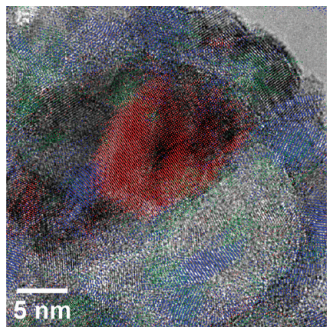

Figure 6. HRTEM image of a 26 nm nanoparticle after oxidation in air at 300 °C for 150 min. The overlaid color layers represent lattice spacings for (red) Ni {200}, (blue) NiO {111}, and (green) NiO {220}. The Ni {111} and NiO {200} planes have approximately the same spacing and were not analyzed.

TABLE 1. Average Native and Critical NiO Shell Thicknesses

sample	t_{native} (nm)	$t_{critical}$ (nm)	Δt (nm)
9 nm	1.6 ± 0.3	3.3 ± 0.8	1.7 ± 0.9
26 nm	1.3 ± 0.2	2.6 ± 0.7	1.3 ± 0.7
96 nm	3.9 ± 1.2	4.6 ± 0.9	0.7 ± 1.5

CuO Nanowire Fragments and Reactions with SiO Supports. In some images, particularly for the 96 nm NPs, there appears to be a bimodal particle distribution. The smaller NPs are actually fragments of CuO nanowires that grew from the Cu TEM grid during heat treatments.[51] (TEM and electron diffraction are provided in the Supporting Information, Figure S-11.) Grids treated at higher temperatures or longer times also show coarsening of the SiO film. No intermediate Ni_xSi_y or $Ni_xSi_yO_z$ compounds are expected, because Ni_xSi_y compounds are not observed in bulk ternary phase diagrams, and the only known equilibrium ternary compound, Ni_2SiO_4, is much less stable than phase-separated NiO and SiO_2.[52] We further note that no nickel silicide or nickel silicate patterns were observed in the SAED measurements.

CONCLUSIONS

Distinct size-dependent behaviors for the NKE in the Ni/NiO system were shown and chiefly originate from two properties of the system: (1) Fast self-diffusion of Ni compared with its rate of diffusion through the

NiO shell results in single voids for the smaller sizes (9 and 26 nm), but multiple voids form in the 96 nm NPs, because self-diffusion is not fast enough to cause the voids to combine into a single void. (2) Prior to void formation, a thin (~3 nm) NiO shell forms symmetrically around the Ni core. For smaller sizes, formation of a single void results in asymmetric nanostructures in which the NiO shell is thickest opposite to the void, because core Ni atoms diffuse away from the void during oxidation. The asymmetry is greater for the 26 nm size, because it has a greater proportion of unoxidized core Ni when the void first forms than the 9 nm NPs.

As expected, oxidation occurs most quickly at elevated temperatures. The conversion mechanism does not appear to be sensitive to temperature, because the final structures do not depend on the oxidation temperature. By choosing an intermediate oxidation temperature and varying the reaction time, partially oxidized Ni(core)/NiO(shell) NPs can be synthesized with good control.

METHODS

Nanoparticle Synthesis. Ni NPs were synthesized using minor modifications of previously reported methods,[17,41] which are based on the method initially developed by the Hyeon group.[53] For all samples, 0.200 g (0.778 mmol) of nickel acetylacetonate ($Ni(acac)_2$, 98%, TCI), 2.0 mL (6.1 mmol) of oleylamine (97%, Pfaltz & Bauer), and 5.0 g of trioctylphosphine oxide (TOPO, 99%, Strem) or 5.0 mL of 1-octadecene (ODE, 90%, Sigma-Aldrich) were combined and heated to 80 °C in a three-necked, round-bottomed flask for 2 h under vacuum to remove oxygen before backfilling with nitrogen. Varying amounts of trioctylphosphine (TOP, 97%, Strem) were injected into the mixture before rapidly heating the solution to 240 °C (~20 °C/min ramp rate) with vigorous stirring.

For 9 nm Ni NPs, the solvent was TOPO, and 0.35 mL (0.78 mmol) of TOP was used. For 26 nm Ni NPs, the solvent was ODE, and 0.30 mL (0.67 mmol) of TOP was used. For 96 nm Ni NPs, the solvent was TOPO, and no TOP was used.

After allowing the NP solution to cool to room temperature, methanol was added to flocculate the NPs, followed by centrifugation to separate the NPs from the solvent and excess ligands. The NPs were repeatedly (one to three times) redispersed in hexanes, flocculated by adding methanol, and isolated by centrifugation. The NPs were stored dispersed in hexanes.

Oxidation Procedure and Characterization. For each size of Ni NPs, a solution in hexanes was sonicated for one minute to improve their dispersion, and the mixture was drop cast onto SiO support films on Cu grids for TEM. The ligands were removed to facilitate oxidation by placing the grids in an ultraviolet light with ozone (UVO) cleaner for 4 min at room temperature. For each heat treatment time and temperature, a different TEM grid was used. Heat treatments were performed in air in a Protherm PC442 tube furnace at 200−500 °C for durations of 1−4 h. (The treatments at 500 °C were omitted for the 9 nm sample, because oxidation was completed quickly at 400 °C. For some samples, treatments at 600 °C were also performed, but the TEM substrates became brittle and fractured upon handling.) Control samples with their ligands removed but no furnace treatments were also prepared.

Bright-field TEM images and selected-area electron diffraction were acquired using a JEOL 2000FX microscope. High-resolution TEM was performed using a JEOL 2010F microscope. The outer diameters and shell thicknesses of the NPs were measured using publicly available ImageJ software.[54] NP diameters were determined by manually measuring the diameter of each particle twice, along orthogonal directions, and then taking the average value for at least 40 NPs. Shell thicknesses were also measured manually for at least 40 NPs. For asymmetric shells on the 26 nm NPs, two sets of thickness measurements were performed, one at the shell's thinnest point, and another on the opposing side at the shell's thickest point (Figure 3, bottom panel). Values of $t_{critical}$ were obtained from measurements of the shell thickness after void formation at its thinnest point, which is the same as $t_{critical}$, because we have shown that the shell thickness at the thinnest point remains constant after void formation. The following samples were used for measuring $t_{critical}$: 9 nm (2 h at 300 °C, 1 h at 400 °C), 26 nm (1.5−2 h at 300 °C, 1 h at 400 °C, 1 h at 500 °C), 96 nm (1 h at 300 °C).

Each colored layer in the HRTEM images of Figure 6 and Figure S-10 in the Supporting Information was obtained from a fast Fourier transform (FFT) of the original image. Symmetric, disk-shaped masks, approximately 1.3 nm^{-1} wide, were separately applied for distances corresponding to the plane spacings for Ni and NiO. An inverse FFT of the masked area was calculated, while discarding information from the unmasked area. The planes were colorized and overlaid to create a color-coded composite.

Acknowledgment. This work was supported by the National Science Foundation (Grant CHE-0943975) and startup funds from North Carolina State University. We thank Tom Rawdanowicz for assistance with TEM.

Supporting Information Available: Selected-area electron diffraction for all NP samples, additional TEM images of partially oxidized Ni NPs and of CuO nanowires grown from the TEM grid. This material is available free of charge *via* the Internet at http://pubs.acs.org

REFERENCES AND NOTES

1. Yin, Y. D.; Rioux, R. M.; Erdonmez, C. K.; Hughes, S.; Somorjai, G. A.; Alivisatos, A. P. Formation of Hollow Nanocrystals through the Nanoscale Kirkendall Effect. *Science* **2004**, *304*, 711–714.
2. Yin, Y. D.; Erdonmez, C. K.; Cabot, A.; Hughes, S.; Alivisatos, A. P. Colloidal Synthesis of Hollow Cobalt Sulfide Nanocrystals. *Adv. Funct. Mater.* **2006**, *16*, 1389–1399.
3. Tracy, J. B.; Weiss, D. N.; Dinega, D. P.; Bawendi, M. G. Exchange Biasing and Magnetic Properties of Partially and Fully Oxidized Colloidal Cobalt Nanoparticles. *Phys. Rev. B* **2005**, *72*, 064404.
4. Chernavskii, P. A.; Pankina, G. V.; Zaikovskii, V. I.; Peskov, N. V.; Afanasiev, P. Formation of Hollow Spheres Upon Oxidation of Supported Cobalt Nanoparticles. *J. Phys. Chem. C* **2008**, *112*, 9573–9578.
5. Keng, P. Y.; Kim, B. Y.; Shim, I. B.; Sahoo, R.; Veneman, P. E.; Armstrong, N. R.; Yoo, H.; Pemberton, J. E.; Bull, M. M.; Griebel, J. J.; *et al.* Colloidal Polymerization of Polymer-Coated Ferromagnetic Nanoparticles into Cobalt Oxide Nanowires. *ACS Nano* **2009**, *3*, 3143–3157.
6. Gao, J. H.; Zhang, B.; Zhang, X. X.; Xu, B. Magnetic-Dipolar-Interaction-Induced Self-Assembly Affords Wires of Hollow Nanocrystals of Cobalt Selenide. *Angew. Chem., Int. Ed.* **2006**, *45*, 1220–1223.
7. Wang, C. M.; Baer, D. R.; Thomas, L. E.; Amonette, J. E.; Antony, J.; Qiang, Y.; Duscher, G. Void Formation During Early Stages of Passivation: Initial Oxidation of Iron Nanoparticles at Room Temperature. *J. Appl. Phys.* **2005**, *98*, 094308.
8. Cabot, A.; Puntes, V. F.; Shevchenko, E.; Yin, Y.; Balcells, L.; Marcus, M. A.; Hughes, S. M.; Alivisatos, A. P. Vacancy Coalescence During Oxidation of Iron Nanoparticles. *J. Am. Chem. Soc.* **2007**, *129*, 10358–10360.
9. Nakamura, R.; Matsubayashi, G.; Tsuchiya, H.; Fujimoto, S.; Nakajima, H. Formation of Oxide Nanotubes *via* Oxidation of Fe, Cu, and Ni Nanowires and Their Structural Stability: Difference in Formation and Shrinkage Behavior of Interior Pores. *Acta Mater.* **2009**, *57*, 5046–5052.
10. Nakamura, R.; Tokozakura, D.; Nakajima, H.; Lee, J. G.; Mori, H. Hollow Oxide Formation by Oxidation of Al and Cu Nanoparticles. *J. Appl. Phys.* **2007**, *101*, 074303.
11. Peng, Q.; Sun, X. Y.; Spagnola, J. C.; Saquing, C.; Khan, S. A.;

Spontak, R. J.; Parsons, G. N. Bi-directional Kirkendall Effect in Coaxial Microtuble Nanolaminate Assemblies Fabricated by Atomic Layer Deposition. *ACS Nano* **2009**, *3*, 546–554.
12. Tokozakura, D.; Nakamura, R.; Nakajima, H.; Lee, J. G.; Mori, H. Transmission Electron Microscopy Observation of Oxide Layer Growth on Cu Nanoparticles and Formation Process of Hollow Oxide Particles. *J. Mater. Res.* **2007**, *22*, 2930–2935.
13. Nakamura, R.; Lee, J. G.; Tokozakura, D.; Mori, H.; Nakajima, H. Formation of Hollow ZnO through Low-Temperature Oxidation of Zn Nanoparticles. *Mater. Lett.* **2007**, *61*, 1060–1063.
14. Chiang, R. K.; Chiang, R. T. Formation of Hollow Ni_2P Nanoparticles Based on the Nanoscale Kirkendall Effect. *Inorg. Chem.* **2007**, *46*, 369–371.
15. Henkes, A. E.; Vasquez, Y.; Schaak, R. E. Converting Metals into Phosphides: A General Strategy for the Synthesis of Metal Phosphide Nanocrystals. *J. Am. Chem. Soc.* **2007**, *129*, 1896–1897.
16. Henkes, A. E.; Schaak, R. E. Trioctylphosphine: A General Phosphorus Source for the Low-Temperature Conversion of Metals into Metal Phosphides. *Chem. Mater.* **2007**, *19*, 4234–4242.
17. Wang, J.; Johnston-Peck, A. C.; Tracy, J. B. Nickel Phosphide Nanoparticles with Hollow, Solid, and Amorphous Structures. *Chem. Mater.* **2009**, *21*, 4462–4467.
18. Hou, H. W.; Peng, Q.; Zhang, S. Y.; Guo, Q. X.; Xie, Y. A "User-Friendly" Chemical Approach Towards Paramagnetic Cobalt Phosphide Hollow Structures: Preparation, Characterization, and Formation Mechanism of Co_2P Hollow Spheres and Tubes. *Eur. J. Inorg. Chem.* **2005**, 2625–2630.
19. Cabot, A.; Smith, R. K.; Yin, Y. D.; Zheng, H. M.; Reinhard, B. M.; Liu, H. T.; Alivisatos, A. P. Sulfidation of Cadmium at the Nanoscale. *ACS Nano* **2008**, *2*, 1452–1458.
20. Cabot, A.; Ibaáñez, M.; Guardia, P.; Alivisatos, A. P. Reaction Regimes on the Synthesis of Hollow Particles by the Kirkendall Effect. *J. Am. Chem. Soc.* **2009**, *131*, 11326–11328.
21. Nakamura, R.; Lee, J. G.; Mori, H.; Nakajima, H. Oxidation Behaviour of Ni Nanoparticles and Formation Process of Hollow NiO. *Philos. Mag.* **2008**, *88*, 257–264.
22. Fan, H. J.; Gösele, U.; Zacharias, M. Formation of Nanotubes and Hollow Nanoparticles Based on Kirkendall and Diffusion Processes: A Review. *Small* **2007**, *3*, 1660–1671.
23. Zhdanov, V. P.; Kasemo, B. On the Feasibility of Strain-Induced Formation of Hollows During Hydriding or Oxidation of Metal Nanoparticles. *Nano Lett.* **2009**, *9*, 2172–2176.
24. Kim, S. W.; Kim, M.; Lee, W. Y.; Hyeon, T. Fabrication of Hollow Palladium Spheres and Their Successful Application to the Recyclable Heterogeneous Catalyst for Suzuki Coupling Reactions. *J. Am. Chem. Soc.* **2002**, *124*, 7642–7643.
25. Cheng, F. Y.; Ma, H.; Li, Y. M.; Chen, J. $Ni_{1-x}Pt_x$ ($x = 0-0.12$) Hollow Spheres as Catalysts for Hydrogen Generation from Ammonia Borane. *Inorg. Chem.* **2007**, *46*, 788–794.
26. Lou, X. W.; Archer, L. A.; Yang, Z. C. Hollow Micro-/Nanostructures: Synthesis and Applications. *Adv. Mater.* **2008**, *20*, 3987–4019.
27. Lou, X. W.; Wang, Y.; Yuan, C. L.; Lee, J. Y.; Archer, L. A. Template-Free Synthesis of SnO_2 Hollow Nanostructures with High Lithium Storage Capacity. *Adv. Mater.* **2006**, *18*, 2325–2329.
28. Chen, J.; Saeki, F.; Wiley, B. J.; Cang, H.; Cobb, M. J.; Li, Z. Y.; Au, L.; Zhang, H.; Kimmey, M. B.; Li, X. D.; *et al.*, Gold Nanocages: Bioconjugation and Their Potential Use as Optical Imaging Contrast Agents. *Nano Lett.* **2005**, *5*, 473–477.
29. Cai, Y. R.; Pan, H. H.; Xu, X. R.; Hu, Q. H.; Li, L.; Tang, R. K. Ultrasonic Controlled Morphology Transformation of Hollow Calcium Phosphate Nanospheres: A Smart and Biocompatible Drug Release System. *Chem. Mater.* **2007**, *19*, 3081–3083.
30. Skumryev, V.; Stoyanov, S.; Zhang, Y.; Hadjipanayis, G.; Givord, D.; Nogués, J. Beating the Superparamagnetic Limit with Exchange Bias. *Nature* **2003**, *423*, 850–853.
31. Martínez-Boubeta, C.; Simeonidis, K.; Angelakeris, M.; Pazos-Pérez, N.; Giersig, M.; Delimitis, A.; Nalbandian, L.; Alexandrakis, V.; Niarchos, D. Critical Radius for Exchange Bias in Naturally Oxidized Fe Nanoparticles. *Phys. Rev. B* **2006**, *74*, 054430.
32. Tracy, J. B.; Bawendi, M. G. Defects in CoO in Oxidized Cobalt Nanoparticles Dominate Exchange Biasing and Exhibit Anomalous Magnetic Properties. *Phys. Rev. B* **2006**, *74*, 184434.
33. Iglesias, Ò.; Labarta, A.; Batlle, X. Exchange Bias Phenomenology and Models of Core/Shell Nanoparticles. *J. Nanosci. Nanotechnol* **2008**, *8*, 2761–2780.
34. Inderhees, S. E.; Borchers, J. A.; Green, K. S.; Kim, M. S.; Sun, K.; Strycker, G. L.; Aronson, M. C. Manipulating the Magnetic Structure of Co Core/CoO Shell Nanoparticles: Implications for Controlling the Exchange Bias. *Phys. Rev. Lett.* **2008**, *101*, 117202.
35. Kavich, D. W.; Dickerson, J. H.; Mahajan, S. V.; Hasan, S. A.; Park, J. H. Exchange Bias of Singly Inverted FeO/Fe_3O_4 Core−Shell Nanocrystals. *Phys. Rev. B* **2008**, *78*, 174414.
36. Vasilakaki, M.; Trohidou, K. N. Numerical Study of the Exchange-Bias Effect in Nanoparticles with Ferromagnetic Core/Ferrimagnetic Disordered Shell Morphology. *Phys. Rev. B* **2009**, *79*, 144402.
37. Ong, Q. K.; Wei, A.; Lin, X.-M. Exchange Bias in Fe/Fe_3O_4 Core−Shell Magnetic Nanoparticles Mediated by Frozen Interfacial Spins. *Phys. Rev. B* **2009**, *80*, 134418.
38. Pang, S. F.; Kurosawa, Y.; Kondo, T.; Kawai, T. Decomposition of Monolayer Coverage on Gold Nanoparticles by UV/Ozone Treatment. *Chem. Lett.* **2005**, *34*, 544–545.
39. Chen, W.; Kim, J.; Sun, S. H.; Chen, S. W. Electro-oxidation of Formic Acid Catalyzed by FePt Nanoparticles. *Phys. Chem. Chem. Phys.* **2006**, *8*, 2779–2786.
40. Aliaga, C.; Park, J. Y.; Yamada, Y.; Lee, H. S.; Tsung, C. K.; Yang, P. D.; Somorjai, G. A. Sum Frequency Generation and Catalytic Reaction Studies of the Removal of Organic Capping Agents from Pt Nanoparticles by UV−Ozone Treatment. *J. Phys. Chem. C* **2009**, *113*, 6150–6155.
41. Johnston-Peck, A. C.; Wang, J. W.; Tracy, J. B. Synthesis and Structural and Magnetic Characterization of Ni(Core)/NiO(Shell) Nanoparticles. *ACS Nano* **2009**, *3*, 1077–1084.
42. Zhang, L.; He, R.; Gu, H. C. Oleic Acid Coating on the Monodisperse Magnetite Nanoparticles. *Appl. Surf. Sci.* **2006**, *253*, 2611–2617.
43. Chen, L.; Chen, J. M.; Zhou, H. D.; Zhang, D. J.; Wan, H. Q. Synthesis of Dodecanethiol Monolayer-Stabilized Nickel Nanoparticles. *Mater. Sci. Eng., A* **2007**, *452*, 262–266.
44. García-Cerda, L. A.; Romo-Mendoza, L. E.; Quevedo-López, M. A. Synthesis and Characterization of NiO Nanoparticles and Their PMMA Nanocomposites Obtained by *in Situ* Bulk Polymerization. *J. Mater. Sci.* **2009**, *44*, 4553–4556.
45. Maier, K.; Mehrer, H.; Lessmann, E.; Schüle, W. Self-Diffusion in Nickel at Low Temperatures. *Phys. Status Solidi B* **1976**, *78*, 689–698.
46. Atkinson, A.; Taylor, R. I. Diffusion of Ni in the Bulk and along Dislocations in NiO Single-Crystals. *Philos. Mag. A* **1979**, *39*, 581–595.
47. José-Yacamán, M.; Gutierrez-Wing, C.; Miki, M.; Yang, D. Q.; Piyakis, K. N.; Sacher, E. Surface Diffusion and Coalescence of Mobile Metal Nanoparticles. *J. Phys. Chem. B* **2005**, *109*, 9703–9711.
48. Chen, Y.; Palmer, R. E.; Wilcoxon, J. P. Sintering of Passivated Gold Nanoparticles under the Electron Beam. *Langmuir* **2006**, *22*, 2851–2855.
49. Latham, A. H.; Wilson, M. J.; Schiffer, P.; Williams, M. E. Tem-Induced Structural Evolution in Amorphous Fe Oxide Nanoparticles. *J. Am. Chem. Soc.* **2006**, *128*, 12632–12633.
50. Latham, A. H.; Williams, M. E. Transmission Electron Microscope-Induced Structural Evolution in Amorphous

Fe, Co, and Ni Oxide Nanoparticles. *Langmuir* **2008**, *24*, 14195–14202.
51. Jiang, X. C.; Herricks, T.; Xia, Y. N. CuO Nanowires Can Be Synthesized by Heating Copper Substrates in Air. *Nano Lett.* **2002**, *2*, 1333–1338.
52. Lee, P. S.; Mangelinck, D.; Pey, K. L.; Ding, J.; Dai, J. Y.; Ho, C. S.; See, A. On the Ni−Si Phase Transformation with/without Native Oxide. *Microelectron. Eng.* **2000**, *51*−*2*, 583–594.
53. Lee, I. S.; Lee, N.; Park, J.; Kim, B. H.; Yi, Y. W.; Kim, T.; Kim, T. K.; Lee, I. H.; Paik, S. R.; Hyeon, T. Ni/NiO Core/Shell Nanoparticles for Selective Binding and Magnetic Separation of Histidine-Tagged Proteins. *J. Am. Chem. Soc.* **2006**, *128*, 10658–10659.
54. Rasband, W. S. Imagej. http://rsb.info.nih.gov/ij/ (accessed June 1, 2009).